JEM Journal of Experimental Medicine

ARTICLE

Hemifacial myohyperplasia is due to somatic muscular PIK3CA gain-of-function mutations and responds to pharmacological inhibition

Charles Bayard[1,2,3*], Eleonora Segna[4*], Maxime Taverne[5*], Antoine Fraissenon[2,6,7,8*], Quentin Hennocq[5], Baptiste Periou[9], Lola Zerbib[1,2,3], Sophia Ladraa[1,2], Célia Chapelle[1,2], Clément Hoguin[2,3], Sophie Kaltenbach[10], Patrick Villarese[10], Vahid Asnafi[1,2,10], Christine Broissand[11], Ivan Nemazanyy[12], Gwennhael Autret[13], Nicolas Goudin[14], Christophe Legendre[1,2,15], François-Jérôme Authier[9], Thomas Viel[13], Bertrand Tavitian[1,13], Cyril Gitiaux[1,16], Sylvie Fraitag[17], Jean-Paul Duong[1,17], Clarisse Delcros[1,2], Bernard Sergent[4], Arnaud Picard[1,4], Michael Dussiot[18], Laurent Guibaud[2,6], Roman Khonsari[1,4,5**], and Guillaume Canaud[1,2,3**]

Hemifacial myohyperplasia (HFMH) is a rare cause of facial asymmetry exclusively involving facial muscles. The underlying cause and the mechanism of disease progression are unknown. Here, we identified a somatic gain-of-function mutation of *PIK3CA* in five pediatric patients with HFMH. To understand the physiopathology of muscle hypertrophy in this context, we created a mouse model carrying specifically a *PIK3CA* mutation in skeletal muscles. *PIK3CA* gain-of-function mutation led to striated muscle cell hypertrophy, mitochondria dysfunction, and hypoglycemia with low circulating insulin levels. Alpelisib treatment, an approved PIK3CA inhibitor, was able to prevent and reduce muscle hypertrophy in the mouse model with correction of endocrine anomalies. Based on these findings, we treated the five HFMH patients. All patients demonstrated clinical, esthetical, and radiological improvement with proof of target engagement. In conclusion, we show that HFMH is due to somatic alteration of *PIK3CA* and is accessible to pharmacological intervention.

Introduction

Hemifacial myohyperplasia (HFMH) is a rare cause of facial asymmetry exclusively involving facial muscles, initially reported as "hypertrophy and asymmetry of the facial muscles" (Lee et al., 2001). This disorder is reported in very few patients in the literature (Castillo Taucher et al., 2003; Pereira-Perdomo et al., 2010; Miranda et al., 2010; Siponen et al., 2007; Zissman et al., 2020). The clinical presentation of HFMH patients is strikingly consistent, with unilateral muscular hypertrophy mimicking spasm and orofacial dystonia, leading to diagnostic errors and inadequate management strategies, including aggressive attempts of surgical correction (Zissman et al., 2020). The genetic causes of HFMH are currently unknown.

The recent discovery of the role played by somatic mutation of genes activating the PIK3CA/AKT/mTOR pathway has opened new treatment perspectives for patients (Canaud et al., 2021). Particularly, *PIK3CA* gain-of-function mutations explain the vast majority of overgrowth syndromes (Canaud et al., 2021). *PIK3CA* encodes the 110-kD catalytic α-subunit of PI3K, a lipid kinase

[1]Université Paris Cité, Paris, France; [2]Institut national de la santé et de la recherche médicale U1151, Institut Necker-Enfants Malades, Paris, France; [3]Unité de Médecine Translationnelle et Thérapies Ciblées, Hôpital Necker-Enfants Malades, Assistance Publique Hôpitaux de Paris, Paris, France; [4]Service De Chirurgie Maxillo-Faciale et Chirurgie Plastique, Hôpital Necker-Enfants Malades, Assistance Publique Hôpitaux de Paris, Paris, France; [5]Laboratoire Forme et Croissance du Crâne, Hôpital Necker-Enfants Malades, Assistance Publique Hôpitaux de Paris, Paris, France; [6]Service d'Imagerie Pédiatrique, Hôpital Femme-Mère-Enfant, Hospices Civils de Lyon, Bron, France; [7]CREATIS Unité mixte de recherche 5220, Villeurbanne, France; [8]Service de Radiologie Mère-Enfant, Hôpital Nord, Saint Etienne, France; [9]Service d'anatomie Pathologique, Hôpital Henri Mondor, Assistance Publique Hôpitaux de Paris, Paris, France; [10]Laboratoire d'Oncohématologie, Hôpital Necker-Enfants Malades, Assistance Publique Hôpitaux de Paris, Paris, France; [11]Pharmacie, Hôpital Necker-Enfants Malades, Assistance Publique Hôpitaux de Paris, Paris, France; [12]Platform for Metabolic Analyses, Structure Fédérative de Recherche Necker, Institut national de la santé et de la recherche médicale Paris, France; [13]Plateforme Imageries du Vivant, Université Paris Cité, Paris Cardiovascular Research Center, Institut national de la santé et de la recherche médicale, Paris, France; [14]Necker Bio-Image Analysis, Institut national de la santé et de la recherche médicale, Paris, France; [15]Service de Néphrologie, Transplantation Adultes, Hôpital Necker-Enfants Malades, Assistance Publique Hôpitaux de Paris, Paris, France; [16]Service de Neurophysiologie Clinique Pédiatrique, Centre de Référence des Pathologies Neuromusculaires, Hôpital Necker-Enfants Malades, Assistance Publique Hôpitaux de Paris, Paris, France; [17]Service d'Anatomie Pathologique, Hôpital Necker-Enfants Malades, Assistance Publique Hôpitaux de Paris, Paris, France; [18]Institut national de la santé et de la recherche médicale U1163, Laboratory of Cellular and Molecular Mechanisms of Hematological Disorders and Therapeutic Implications, Laboratoire d'Excellence GR-Ex, Paris, France.

*C. Bayard, E. Segna, M. Taverne, and A. Fraissenon contributed equally to this paper; **R. Khonsari and G. Canaud contributed equally to this paper. Correspondence to Guillaume Canaud: guillaume.canaud@inserm.fr; Roman Khonsari: roman.khonsari@aphp.fr.

that controls signaling pathways involved in cell proliferation, motility, survival, and metabolism (Madsen and Vanhaesebroeck, 2020). Post-zygotic mosaic gain-of-function *PIK3CA* mutations result in protein activation, leading to abnormal cellular proliferation, tissue hyperplasia, and organ overgrowth. The understanding of the genetic bases of overgrowth has enabled the treatment of patients presenting *PIK3CA*-related overgrowth syndromes (PROS) with a specific PI3K inhibitor (BYL719, alpelisib), initially designed as an antineoplastic drug (Venot et al., 2018). Alpelisib is efficiently tackling soft-tissue overgrowth in PROS (Venot et al., 2018; Ladraa et al., 2022; Delestre et al., 2021; Morin et al., 2022).

We hypothesized that the PIK3CA/AKT/mTOR pathway was abnormally affected in patients with HFMH. Here, we report the results of the clinical screening, mechanistic investigations, and treatment of five patients with HFMH.

Results

PIK3CA gain-of-function mutations explain HFMH

We identified five pediatric patients, including three girls, ranging from 4 to 15 yr old with clinical presentation of HFMH (Fig. 1 and Fig. S1). In more detail, 5/5 patients had chin skin dimpling and small nasal vestibule, 4/5 had chin deviation, dysmorphic ear, narrow palpebral fissure, and eyebrow ptosis, 3/5 had lip commissure canting, and finally, 3/5 had nasal deviation. All patients had magnetic resonance imaging (MRI) demonstrating muscular hypertrophy affecting in various combinations facial, masticatory (pterygoids and masseter), and neck (scalene and sternocleidomastoid) muscles (Fig. 1). All patients had benefited from computerized tomography (CT) scan imaging before HFMH diagnosis that showed bone anomalies in 4/5 cases including mild chin deviation in 3/4 and major skeletal deformation with homolateral maxillary and mandibular growth impairment in 1/5. All patients had available electroneuromyography assessments that showed normal results, including normal blink reflex responses and needle electromyogram of facial muscles.

2/5 patients had been treated with botulinum toxin with injections performed every 6 mo. Patient 5 benefited from three injections in mentalis, zygomaticus minor, and major and orbicularis oculi muscles (130 then twice 200 I.U.), and patient 3 benefited from nine injections in the same three muscles (I.U. injected from 50 to 400). For both patients, no relevant esthetic or functional results were observed.

We performed muscular biopsies from the affected zones (oral mucosa, buccinator muscle, and masseter muscle) in 5/5 patients, under general or local anesthesia depending on age, through an intraoral approach. Standard histology was normal. Genotyping of the biopsies revealed the presence of *PIK3CA* variants in all tested samples. Pathogenic *E545K* variant was found in patient 1 and 5 with a variant allelic frequency (VAF) of 15% and 14%, respectively. The *E542K* variant was detected in patient 3 (VAF 12%) and 4 (VAF 21%). Lastly, the *H1047R* variant was identified in patient 2 (VAF 25%; Table 1). All variants were already characterized as pathogenic (Canaud et al., 2021).

Thus, we concluded that *PIK3CA* gain-of-function mutations explained all five HFMH cases.

A mouse model of PIK3CA gain-of-function mutations in skeletal muscles

To gain insight into the mechanisms of *PIK3CA*-related muscle overgrowth, we designed a mouse model carrying specifically a *PIK3CA* gain-of-function mutation in striated muscle. To this aim, we interbred the R26StopFLP110* mouse strain with HSA Cre mice to generate $PIK3CA^{HSA\text{-}CreER}$ animals that express a constitutively overactivated form of PIK3CA upon tamoxifen administration. To follow Cre recombination, $PIK3CA^{HSA\text{-}CreER}$ mice were then interbred with Gt(ROSA)26Sortm4(ACTB-tdTomato-EGFP)Luo/J mice. In all tissues, these mice express a cell-membrane-localized tdTomato fluorescent protein that is replaced by GFP after *Cre* recombination.

To overcome developmental issues, we used 6-wk-old mice that were treated with a daily dose of 40 mg.kg-1 tamoxifen for 5 d to induce Cre recombination. We observed that starting 3 wk after *Cre* recombination, $PIK3CA^{HSA\text{-}CreER}$ mice progressively gained weight compared with their wild-type littermates ($PIK3CA^{WT}$; Fig. 2 A). This was the case for both males and females. Around 11 wk after induction in males and 24 wk in females, body weight of control mice became higher than in $PIK3CA^{HSA\text{-}CreER}$ (Fig. 2 A). Whole-body MRI at 15 wk after tamoxifen revealed skeletal muscle hypertrophy in $PIK3CA^{HSA\text{-}CreER}$ mice that was approximately twice as in controls (Fig. 2, B and C). Fat content in $PIK3CA^{HSA\text{-}CreER}$ was significantly reduced compared with controls (Fig. 2, B and C). Skeletal muscle hypertrophy was associated with gain in muscle strength compared with controls (Fig. 2 D).

We sacrificed 20 controls and 20 $PIK3CA^{HSA\text{-}CreER}$ mice 15 wk after tamoxifen administration. Necropsy examination confirmed diffuse skeletal muscle hypertrophy with adipose tissue shrinkage compared with control littermates (Fig. 2 E). We confirmed that mutant p110α (p110*) and GFP were expressed in striated muscles of $PIK3CA^{HSA\text{-}CreER}$ mice (Fig. 2, F and G). Histological examination revealed hypertrophic striated cells (Fig. 2 H and Fig. S2, A–D). We did not observe any other histological anomalies. Western blot and immunofluorescence studies showed AKT/mTOR pathway activation in striated muscles of $PIK3CA^{HSA\text{-}CreER}$ mice (Fig. 2, I and J). Mechanistically, PIK3CA is involved in cell growth and proliferation but KI67 immunostaining did not show hyperplasia (Fig. 2 K). However, using the Amnis ImageStream system, we confirmed that cells isolated from striated muscle of $PIK3CA^{HSA\text{-}CreER}$ mice were hypertrophic compared with controls (Fig. 2 L). Blood cell count did not reveal any anomalies (Fig. S2 E). However, we observed that $PIK3CA^{HSA\text{-}CreER}$ mice were hypoglycemic compared with controls (Fig. 2 M). We recently identified an endocrine loop leading to chronic hypoglycemia in another mouse model carrying specifically *PIK3CA* gain-of-function mutation in adipose tissue (Ladraa et al., 2022). Indeed, *PIK3CA* gain-of-function mutation led to permanent glucose transporters addressing the cell membrane, allowing glucose entry and subsequent hypoglycemia. The latter reduced insulin secretion, which in turn dramatically increased insulin-like growth factor binding protein production followed by liver IGF-1 sequestration and a reduction in IGF-1 circulating levels similar to clinical observations. We obtained similar results in

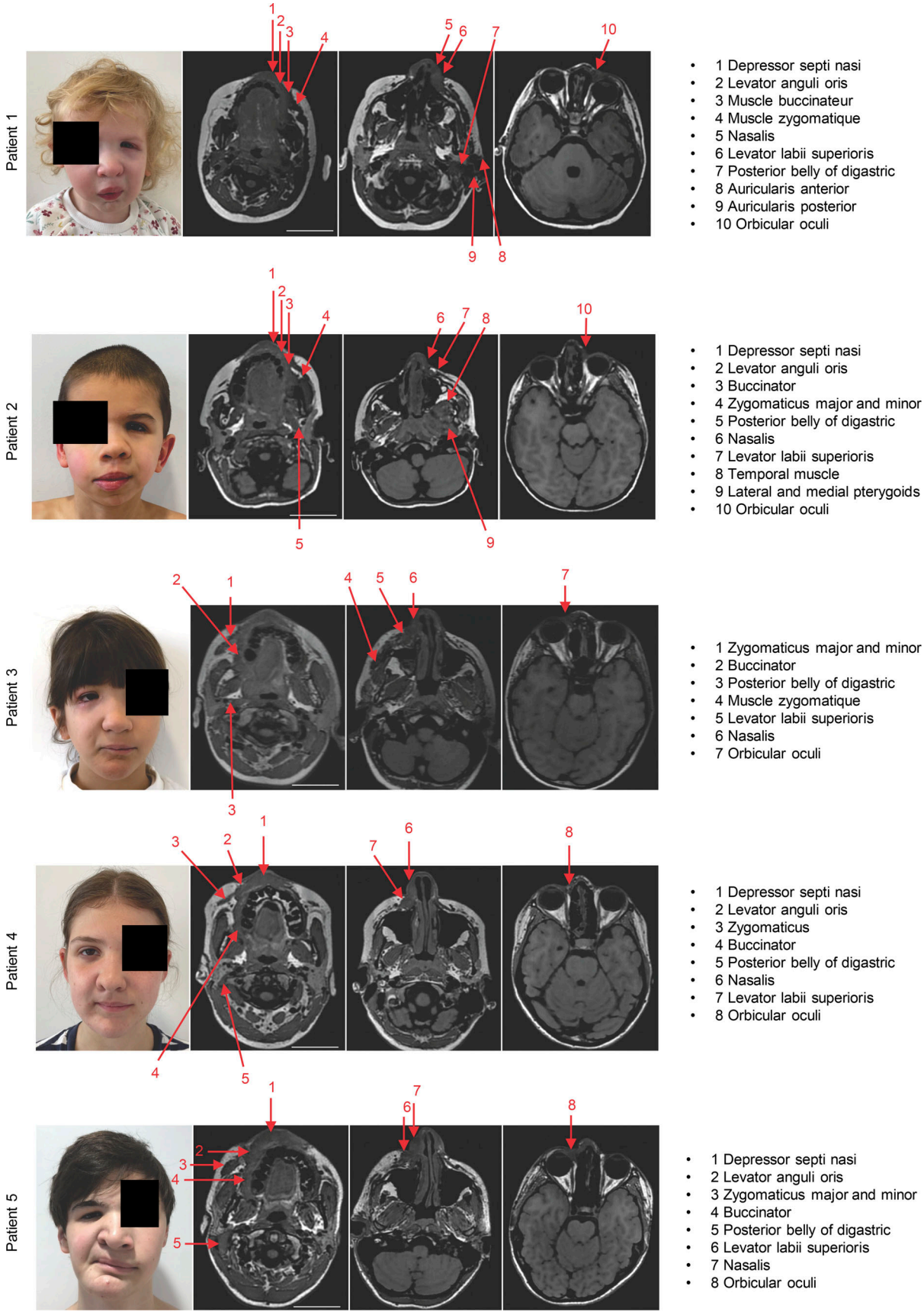

Figure 1. **Patients with hemifacial myohyperplasia.** Representative photographs of the five patients and affected muscles assessed with MRI. Scale bar: 5 cm.

Table 1. **Patient characteristics**

	Patient 1	Patient 2	Patient 3	Patient 4	Patient 5
Age, year	4	6	9	14	15
Specimen used for genotyping	Muscle	Muscle	Muscle	Muscle	Muscle
DNA changes	c.1633G>A	c.3140A>G	c.1624G>A	c.1624G>A	c.1633G>A
VAF (%)[a]	15	25	12	21	14
Amino acid change	p.Glu545Lys	p.His1047Arg	p.Glu542Lys	p.Glu542Lys	p.Glu545Lys
COSMIC[b] genomic mutation ID	COSV55873239	COSV55873195	COSV55873227	COSV55873227	COSV55873239
Treatments prior to alpelisib	-	-	Botulinum toxin injections	-	Botulinum toxin injections

[a]Corresponds to the percentage of alternate or mutant reads to total reads detected by next-generation sequencing.
[b]Catalogue of Somatic Mutations in Cancer.

PIK3CA$^{HSA\text{-}CreER}$ mouse model with low insulin and IGF1 levels (Fig. 2, M and O; and Fig. S2 F) but conserved insulin secretion capacities as demonstrated using oral glucose tolerance test (GTT; Fig. 2 P). Consistently, positron emission tomography and computed tomography (PET-CT) scan showed higher fluoro-D-glucose (FDG) muscular uptake in *PIK3CA*$^{HSA\text{-}CreER}$ mice compared with controls (Fig. 2 Q).

Mitochondria play a major role in energy for striated muscle metabolism. PI3K has been involved in mitochondrial function (Li et al., 2019); we therefore explored the impact of *PIK3CA* gain-of-function on mitochondria number and activity in the *PIK3CA*$^{HSA\text{-}CreER}$ mouse model. Flow cytometry of isolated striated muscle cells revealed alteration in the mitochondrial transmembrane potential as assessed by tetramethylrhodamine ethyl ester (TMRE) staining with reduced Mitotracker expression (Fig. 2, R and S). 10-N-nonyl acridine orange (NAO) staining showed reduced mitochondrial mass in striated muscle cells of *PIK3CA*$^{HSA\text{-}CreER}$ compared with controls (Fig. 2 T). Plasma metabolites metabolomics analysis revealed energy production with increased ATP production with mitochondria and anabolic activities (Fig. S3).

Hence, we created a mouse model of PIK3CA-related skeletal muscle overgrowth affecting the gross morphology, cellular structure, and function of striated muscles.

Alpelisib improves PIK3CA$^{HSA\text{-}CreER}$ mouse model

We recently identified alpelisib (BYL719), a PIK3CA inhibitor, as a promising treatment for patients with PROS, and very recently this drug has been approved by the US FDA for patients with PROS (over 2 yr of age; Venot et al., 2018). We decided to test whether this molecule was efficient at improving skeletal muscle overgrowth in our mouse model. To this end, we used two different approaches. We first administered alpelisib daily starting 48 h after *Cre* induction as a preventive study. We observed that alpelisib-treated *PIK3CA*$^{HSA\text{-}CreER}$ mice had an overtly normal appearance during the 22 wk of treatment and a body weight increase similar to that of controls (Fig. 3 A). MRI performed 8 wk after alpelisib initiation showed no skeletal muscle overgrowth compared with vehicle *PIK3CA*$^{HSA\text{-}CreER}$-treated mice (Fig. 3, B and C). Mice were then sacrificed and a necropsy examination confirmed that alpelisib-treated *PIK3CA*$^{HSA\text{-}CreER}$ mice had no muscle hypertrophy and were indistinguishable from controls. Histology showed no difference between *PIK3CA*$^{HSA\text{-}CreER}$ mice treated with preventive alpelisib and *PIK3CA*^{WT} mice (Fig. 3 D). Western blot and immunofluorescent studies showed blunted AKT and S6RP phosphorylation (Fig. 3, E and F). *PIK3CA*$^{HSA\text{-}CreER}$ mice treated with preventive alpelisib demonstrated normal 12-h fasted glycemia compared with *PIK3CA*$^{HSA\text{-}CreER}$ vehicle–treated mice (Fig. 3 G). Consistently, insulin and IGF-1 circulating levels were corrected (Fig. 3, H and I).

Next, we administered alpelisib to *PIK3CA*$^{HSA\text{-}CreER}$ mice 2 wk after *Cre* induction when global muscle hypertrophy was already prominent for 20 additional weeks, as a therapeutic study. Following alpelisib introduction, we noticed a rapid body weight decrease in alpelisib-treated *PIK3CA*$^{HSA\text{-}CreER}$ mice compared with control (Fig. 3 A). MRI performed at 8 wk showed significant reduction in muscular volume compared with *PIK3CA*$^{HSA\text{-}CreER}$ vehicle mice (Fig. 3, B and C; and Fig. S2, B–D). Similar to previous experiments with early alpelisib introduction, we observed that the histology of the striated muscle of *PIK3CA*$^{HSA\text{-}CreER}$ mice treated in the therapeutic study was conserved (Fig. 3 D), with reduced phosphorylation of the AKT and S6RP proteins (Fig. 3, E and F). Blood glucose, insulin, and IGF-1 circulating levels were increased in the therapeutic alpelisib group (Fig. 3, G–I).

Alpelisib treatments were associated with a partial correction of the different metabolomic anomalies (Fig. S4, A and B).

We then concluded that alpelisib was efficient at both preventing and treating PIK3CA-related striated muscle hypertrophy.

Alpelisib improves patients with PIK3CA-related skeletal muscle overgrowth

Based on the preclinical data, we decided to treat the five HFMH pediatric patients with alpelisib. We obtained the authorization from the French regulatory agency (Agence nationale de sécurité du médicament et des produits de santé) and administered a daily dose of 50 mg per day for each patient. Following alpelisib introduction, we noticed in the five patients clinical meaningful hemifacial volume reduction with softer tissues within 3–4 wk (Fig. 4 A). Based on 2D photography quantification, we confirmed the lowering of the lip commissure, the widening of the palpebral fissure, the reduction of nose and chin deviation, and a

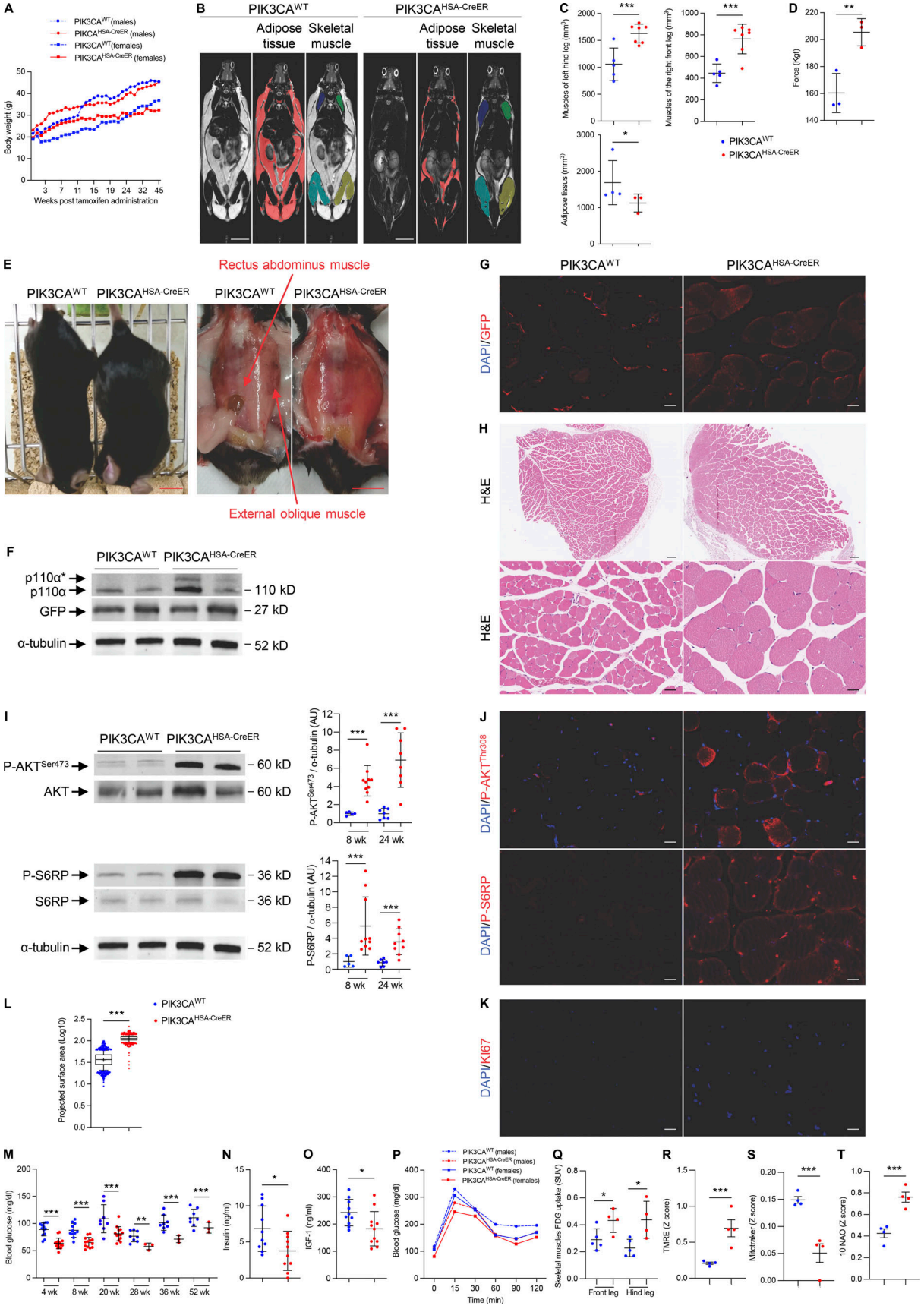

Figure 2. **A mouse model of *PIK3CA*-related skeletal muscle overgrowth. (A)** Male and female body weights of *PIK3CA*^{WT} and *PIK3CA*$^{HSA\text{-}CreER}$ (n = 15 per group) mice following *Cre* recombination. **(B)** Coronal whole-body T2-weighted magnetic resonance images of *PIK3CA*^{WT} and *PIK3CA*$^{HSA\text{-}CreER}$ mice. Scale bar:

1 cm. **(C)** Adipose tissue and skeletal muscle volume quantification. **(D)** Strength measured using grip test (n = 3 per group). **(E)** Representative pictures of *PIK3CA*^{WT} and *PIK3CA*$^{HSA\text{-}CreER}$ mice. Scale bar: 1 cm. **(F)** Western blot of p110α and GFP in skeletal muscles of *PIK3CA*^{WT} and *PIK3CA*$^{HSA\text{-}CreER}$ mice (n = 3 per group). **(G)** Representative GFP immunofluorescence in skeletal muscles of *PIK3CA*^{WT} and *PIK3CA*$^{HSA\text{-}CreER}$ mice. Scale bar: 10 µm. **(H)** Representative H&E staining of striated muscles of *PIK3CA*^{WT} and *PIK3CA*$^{HSA\text{-}CreER}$ mice. Scale bar: 20 µm. **(I)** Western blot of P-AKT^{Ser473}, total AKT, P-S6RP, and S6RP in skeletal muscles of *PIK3CA*^{WT} and *PIK3CA*$^{HSA\text{-}CreER}$ mice and quantification at 8 and 24 wk of age (n = 5–10 mice per group). **(J)** Representative immunofluorescence of P-AKT^{Thr308} and P-S6RP in skeletal muscle of *PIK3CA*^{WT} and *PIK3CA*$^{HSA\text{-}CreER}$ mice. Scale bar: 10 µm. **(K)** Representative immunofluorescence of KI67 in skeletal muscle of *PIK3CA*^{WT} and *PIK3CA*$^{HSA\text{-}CreER}$ mice. Scale bar: 10 µm. **(L)** Quantification of skeletal muscle cell area of *PIK3CA*^{WT} and *PIK3CA*$^{HSA\text{-}CreER}$ mice (n = 5 mice per group). **(M)** 12-h fasted glycemia in *PIK3CA*^{WT} and *PIK3CA*$^{HSA\text{-}CreER}$ mice (n = 5–13 mice per group). **(N)** Insulin circulating levels in *PIK3CA*^{WT} and *PIK3CA*$^{HSA\text{-}CreER}$ mice (n = 10 per group). **(O)** Circulating IGF-1 levels in *PIK3CA*^{WT} and *PIK3CA*$^{HSA\text{-}CreER}$ mice (n = 10–11 per group). **(P)** Oral tolerance test (GTT) in *PIK3CA*^{WT} and *PIK3CA*$^{HSA\text{-}CreER}$ mice (n = 6 mice per group). **(Q)** 18F-FDG uptake in skeletal muscle of *PIK3CA*^{WT} and *PIK3CA*$^{HSA\text{-}CreER}$ mice (n = 4 per group). **(R–T)** (R) TMRE, (S) Mitotracker, and (T) 10 NAO staining in skeletal muscle of *PIK3CA*^{WT} and *PIK3CA*$^{HSA\text{-}CreER}$ mice (n = 4 per group). Data are shown as mean ± SEM. *P < 0.05, **P < 0.01, ***P < 0.001 (two-tailed unpaired t test). Each dot represents one mouse. Data are representative of at least two independent experiments. Of note, all blots from this figure originate from the same gel. Source data are available for this figure: SourceData F2.

better skin texture with a decrease of dimpling effects. 3D photography follow-up before and after treatment initiation was available in three patients (1, 3, and 5). Two-blocks partial least-squares regressions (PLS2B) analysis showed a strong covariation between facial shape and treatment duration in two out of three patients (Fig. 4 B and Fig. S5). In 3/3 patients, the hypertrophic regions were preferentially improved by treatment (Fig. 4 B and Fig. S5).

MRI performed 6 mo after drug introduction showed a modest mean muscular volume reduction of 2.56% (Fig. 4 C). During the study, the drug was well tolerated with no adverse events reported by patients and parents. Since we used a standard dose of alpelisib (50 mg per day) in the five patients while their body weights and ages were different, we decided to explore AKT activity in the affected skeletal muscles after 6 mo on the treatment. We obtained a biopsy in four out of five patients (patients 2–5). Immunofluorescence studies revealed increased AKT and S6RP phosphorylation in the biopsies from 4/4 patients compared with healthy controls (Fig. 4, D–F). Following drug introduction, we observed that AKT and S6RP phosphorylation were blunted demonstrating that alpelisib penetrated into skeletal muscles at this dose in 4/4 patients (Fig. 4, D–F).

In parallel, we performed an unbiased approach of circulating plasma metabolites before and 6 mo following alpelisib introduction. We observed significant changes in key metabolite levels involved in mitochondria and anabolic activities (Fig. 5).

Discussion

Here, we report for the first time that HFMH is due to a somatic gain-of-function mutation of *PIK3CA* in striated muscles and indeed, belongs to the *PIK3CA*-related disorder spectrum. We further created a mouse model harboring a *PIK3CA* gain-of-function mutation in striated muscles that demonstrates muscle overgrowth. We finally showed that mouse and patient striated muscles are sensitive to PIK3CA inhibition using alpelisib.

HFMH has long been standing without molecular explanation. All 5/5 patients in our cohort carried a somatic variant of *PIK3CA*. From a disease mechanism point of view, these mutations make sense since PIK3CA is a major actor of cell growth (Madsen and Vanhaesebroeck, 2020). This was confirmed by the *PIK3CA*$^{HSA\text{-}CreER}$ mice that demonstrated increased skeletal muscle volumes and strength. PIK3CA activation in mice skeletal muscles induced anabolic activities and mitochondrial changes. Identification of *PIK3CA* mutations opens new therapeutic perspectives for HFMH patients since surgical management, botulinum toxin injections, and physical therapy are currently the only treatment solutions and seem to be associated with little to no efficiency. Interestingly, two patients were previously unsuccessfully treated with botulinum toxin injection and demonstrated some degree of response to alpelisib. Since alpelisib benefited from an accelerated US FDA approval for patients with PROS, our work identifies a new patient population that may benefit from the drug. In these potential new alpelisib indications, it is important to determine the affected tissues that are sensitive to PIK3CA inhibition such as we recently reported in lymphatic vessels (Delestre et al., 2021; Morin et al., 2022) and adipocytes (Ladraa et al., 2022). Here, for the first time, to monitor drug efficacy, we performed secondary biopsies 6 mo after drug introduction, and tissue analyses revealed AKT inhibition in all tested patients demonstrating that low doses of alpelisib were sufficient to achieve target inhibition.

One limitation of this study is that the transgene utilized in our mouse model is not found in human pathology. However, it possesses significant potency in activating the AKT/mTOR pathway and overcoming mouse resistance to the *PIK3CA* human variant (Venot et al., 2018).

In conclusion, in this study, we precise the clinical presentation of a little-known syndrome and determine its molecular bases. We further expand the phenotypic spectrum of PROS, we detail the effects of PIK3CA hyperactivity on skeletal muscles using a mouse model, and we show that PIK3CA inhibition seems to be a promising option for treating patients with HFMF, based both on shape quantification and functional assessments. Further investigations are required to establish a more precise determination of the frequency of *PIK3CA* mutation in HFMF, and the encouraging clinical results obtained using alpelisib will have to be confirmed in larger studies.

Materials and methods

Animals

Following previously described procedures (Delestre et al., 2021), we interbred homozygous *R26StopFLP110** (Stock# 012343) mice with *HSA Cre-ER* mice (Stock# 025750), both obtained from The Jackson Laboratory. We obtained *R26StopFLP110*+/−* x *HSA Cre-ER+* (henceforth *PIK3CA*$^{HSA\text{-}CreER}$) and *R26StopFLP110*+/−* x *HAS Cre-ER−* (henceforth *PIK3CA*^{WT}) littermate mice. The p110* protein

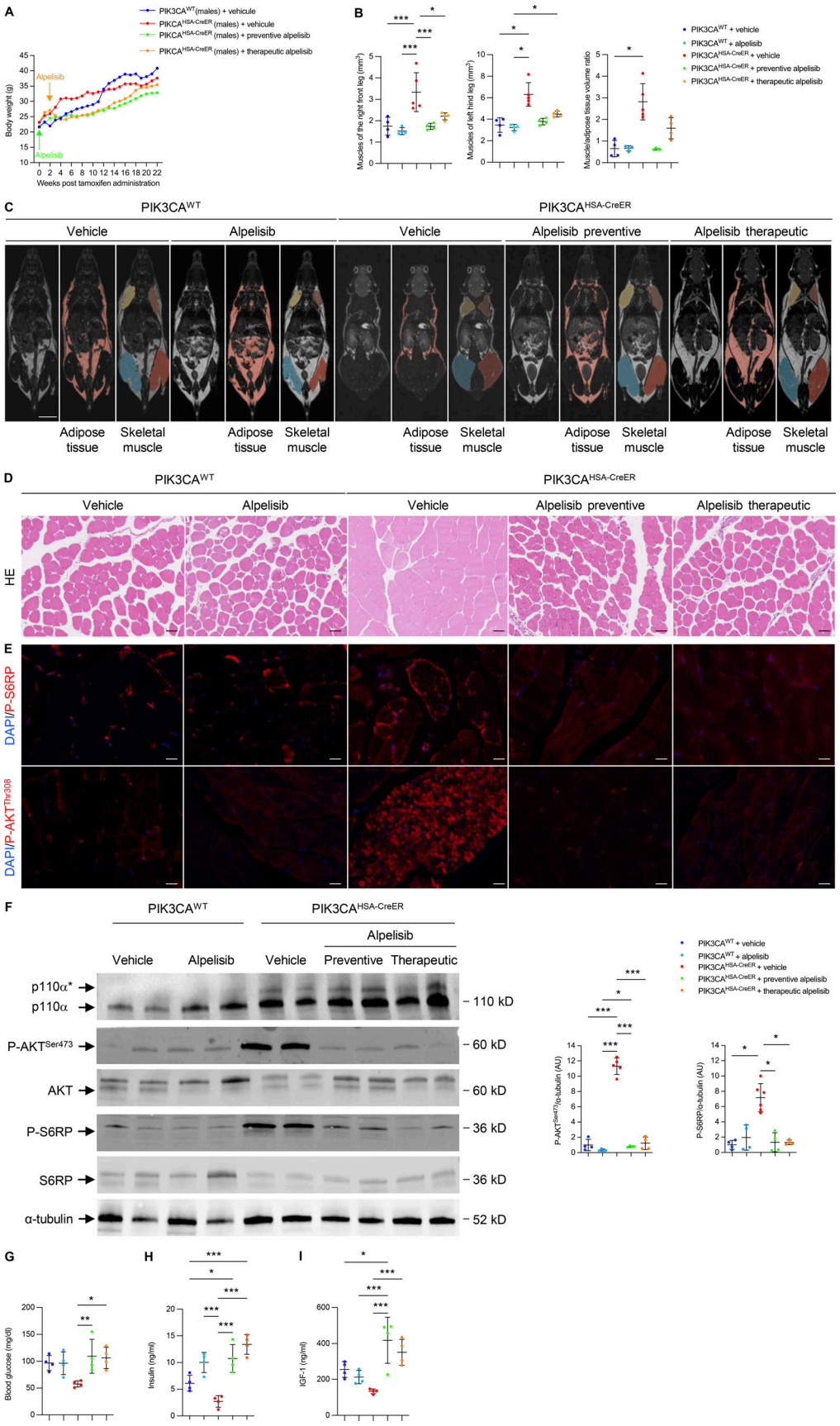

Figure 3. **Alpelisib prevents and reverses skeletal muscle overgrowth in *PIK3CA*$^{HSA\text{-}CreER}$ mice. (A)** Male body weights of *PIK3CA*^{WT} (n = 6) and *PIK3CA*$^{HSA\text{-}CreER}$ treated with either vehicle (n = 12) or preventive (n = 12) or curative alpelisib (n = 12). **(B)** Skeletal muscle and adipose tissue volume quantification. **(C)** Whole-body

T2-weighted magnetic resonance images of *PIK3CA*^{WT} treated either with vehicle (n = 4) or alpelisib (n = 4), *PIK3CA*$^{HSA\text{-}CreER}$ vehicle-treated (n = 5), *PIK3CA*$^{HSA\text{-}CreER}$-treated with preventive alpelisib (n = 4), and *PIK3CA*$^{HSA\text{-}CreER}$-treated with therapeutic alpelisib (n = 4) mice. Scale bar: 1 cm. **(D)** Representative H&E staining of skeletal muscle of *PIK3CA*^{WT} and *PIK3CA*$^{HSA\text{-}CreER}$ mice treated with either vehicle or preventive or curative alpelisib. Scale bar: 10 µm. **(E)** Representative immunofluorescence of P-AKT^{Thr308} and P-S6RP in skeletal muscle of *PIK3CA*^{WT} and *PIK3CA*$^{HSA\text{-}CreER}$ mice treated with either vehicle or alpelisib. Scale bar: 10 µm. **(F)** Western blot and quantification of P110, P-AKT^{Ser473}, AKT, P-S6RP, and S6RP in skeletal muscle of *PIK3CA*^{WT} and *PIK3CA*$^{HSA\text{-}CreER}$ mice treated with either vehicle or alpelisib (n = 4–5 mice per group). **(G)** 12-h fasted glycemia in *PIK3CA*^{WT} and *PIK3CA*$^{HSA\text{-}CreER}$ mice treated with vehicle, preventive, or curative alpelisib (n = 4 mice per group). **(H and I)** (H) Insulin and (I) IGF-1 circulating levels in *PIK3CA*^{WT} and *PIK3CA*$^{HSA\text{-}CreER}$ mice treated with vehicle, preventive, or curative alpelisib (n = 4 mice per group). Data are shown as mean ± SEM. *P < 0.05, **P < 0.01, ***P < 0.001 (ANOVA, followed by the Tukey–Kramer post hoc test). Each dot represents one mouse. Data are representative of at least two independent experiments.

expressed by *R26StopFLP110** mice is a constitutively active chimera that contains the iSH2 domain of p85 fused to the NH2-terminus of p110 via a flexible glycine linker (Klippel et al., 1996). To generate tissue-specific p110*-transgenic mice, a cloned loxP-flanked neoR-stop cassette was inserted into a modified version of pROSA26-1, followed by cDNA encoding p110* and then a frt-flanked IRES-EGFP cassette and a bovine polyadenylation sequence (*R26StopFLP110**; Srinivasan et al., 2009). To follow *Cre* recombination, *PIK3CA*^{WT} and *PIK3CA*$^{HSA\text{-}CreER}$ mice were then interbred with *Gt(ROSA)26Sor*$^{tm4(ACTB\text{-}tdTomato,\text{-}EGFP)Luo/J}$ mice (Muzumdar et al., 2007; Delestre et al., 2021). These mice express a cell membrane–localized tdTomato fluorescent protein in all tissues that is replaced by GFP after *Cre* recombination. All mice used were on a C57BL/6 background.

Animals were fed ad libitum and housed at a constant ambient temperature in a 12-h light cycle. Animals were fed regular chow food (2018 Teklad global 18% protein rodent diets, 3.1 Kcal/g; Envigo). Animal procedures were approved by the Ministère de l'Enseignement Supérieur, de la Recherche et de l'Innovation (APAFIS N°20439-2018121913526398 and 2021110914486827). All appropriate procedures were followed to ensure animal welfare.

At the age of 6 wk, *PIK3CA*^{WT} and *PIK3CA*$^{HSA\text{-}CreER}$ mice received a daily dose of 40 mg.kg^{-1} tamoxifen for 5 consecutive days to induce Cre recombination. Tamoxifen was administered through oral gavage.

PIK3CA^{WT} and *PIK3CA*$^{HSA\text{-}CreER}$ mice were treated with the PIK3CA inhibitor alpelisib (MedChem Express; 50 mg.kg^{-1} in 0.5% carboxymethylcellulose [Sigma-Aldrich], daily oral gavage) or vehicle (0.5% carboxymethylcellulose [Sigma-Aldrich], daily oral gavage). Treatment was started either immediately (preventive study) or 6 wk (therapeutic study) following *Cre* induction. The last dose of alpelisib or vehicle was administered ∼3 h before sacrifice.

All mice were fasted for 12 h before blood glucose measurement (Accuchek Performa; Roche Diagnostic), MRI, and sacrifice.

Grip test

Grip strength performance of the mice was evaluated using a grip strength dynamometer obtained from Bioseb. To assess hindlimb muscle strength, the mice were positioned on a grid surface. Gentle traction was applied to the mice's tails in the opposite direction, and the maximum strength exerted by each mouse before releasing its grip was measured five times. A recovery period of 30 s was provided between each measurement. The average value from the five measurements was calculated as the indicator of hindlimb grip strength.

MRI evaluation

All images were acquired with a 4.7-T small-animal MRI system (BioSpec USR47/40; Bruker BioSpin) on the Plateforme Imageries du Vivant, Université de Paris, Paris Cardiovascular Research Center, Institut national de la santé et de la recherche médicale, Paris, France. Mice underwent whole-body MRI using 3D T2-weighted sequences with and without fat saturation. Volumetric evaluation by MRI was performed with 3D Slicer software (Fedorov et al., 2012) and IntelliSpace Portal software (Philips Healthcare). Whole-body adipose tissue segmentation was obtained by thresholding on a T2-weighted sequence and then removing hypersignal related to water on a T2-weighted sequence with fat saturation. Muscles of each limb were manually segmented according to their low signal intensity and anatomy on a T2-weighted sequence. For both adipose and muscle tissues, volume was calculated by summing images based on 2D contours and slice thickness.

FDG PET-CT imaging

Mice were fasted overnight with free access to water. Mice were then anesthetized (2 ± 0.5% isoflurane in dioxygen) and weighed, and glycemia was measured in blood drawn from the caudal ventral artery using an Accu-Chek Aviva Nano A (Accu-Chek). A 29G needle catheter (Thermo Fischer Scientific) connected to 5 cm polyethylene tubing (Tygon Microbore Tubing, 0.010" × 0.030" OD; Thermo Fisher Scientific) was inserted into the caudal vein for radiotracer injection. 9.2 ± 1.5 MBq of 2′-deoxy-2′-[18F]FDG (Advanced Applied Applications) in 0.2 ml saline was injected via the catheter. Mice were left awake in their cage for 45 min and then installed into the PET-CT dedicated bed. Respiration and body temperature were registered. Body temperature was maintained at 34 ± 2°C and anesthesia was controlled according to the breathing rate throughout the entire PET-CT examination. CT was acquired in a PET-CT scanner (nanoScan PET-CT; Mediso Medical Imaging Systems) using the following acquisition parameters: semicircular mode, 50 kV tension, 720 projections full scan, 300 ms per projection, and binning 1:4. CT projections were reconstructed by filtered retroprojection (filter: cosine; cutoff: 100%) using Nucline 3.00.010.0000 software (Mediso Medical Imaging Systems). 55 min after tracer injection, PET data were collected for 10 min in list mode and binned using a 5-ns time window with a 400–600 keV energy window and a 1:5 coincidence mode. Data were reconstructed using the Tera-Tomo reconstruction engine (3D-OSEM-based manufactured customized algorithm) with expectation maximization iterations, scatter, and attenuation correction. Volumes of interest were delineated on the organs

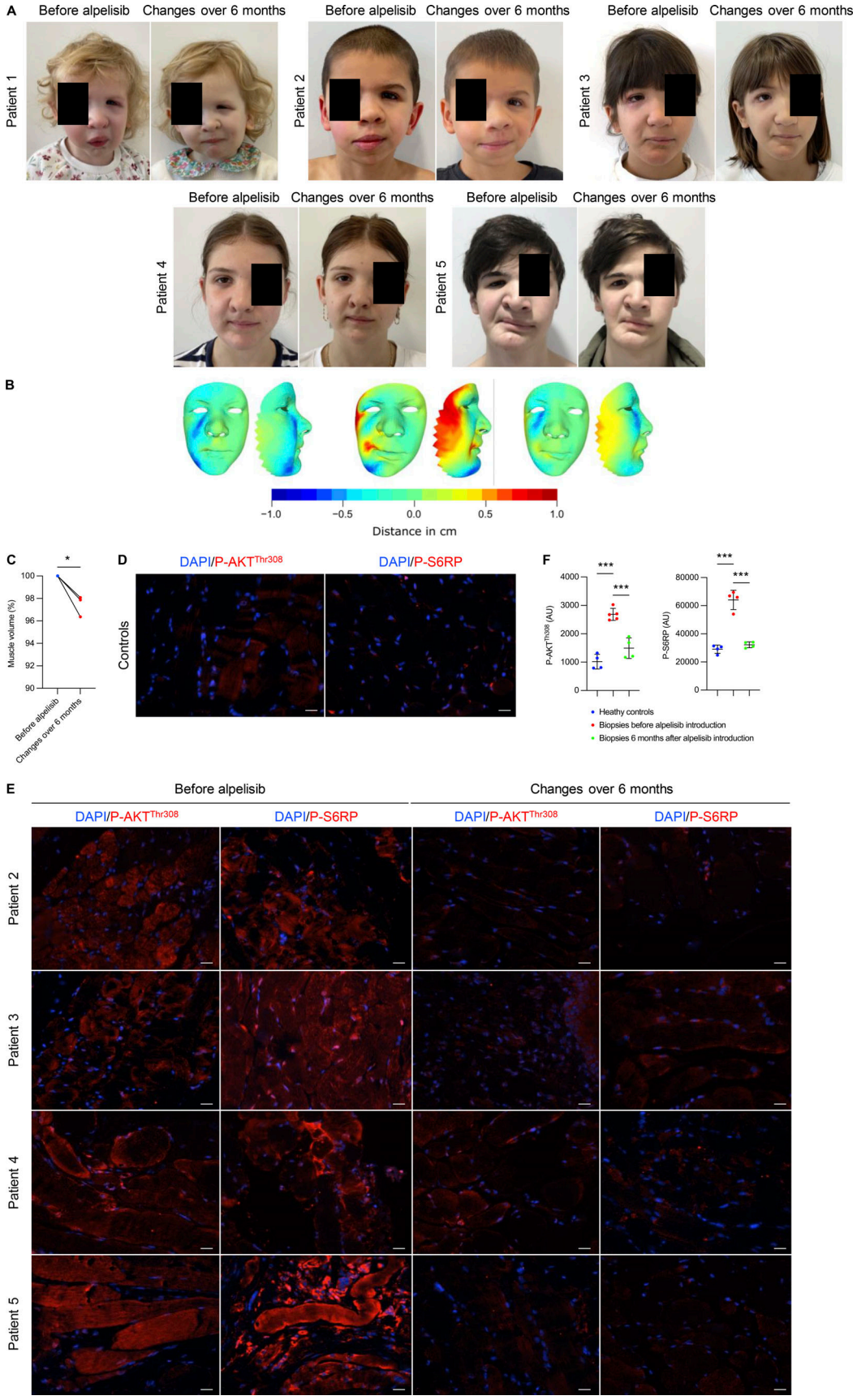

Figure 4. **Alpelisib improves hemifacial myohyperplasia phenotype in patients. (A)** Photographs of the five patients before and 6 mo after alpelisib introduction. **(B)** 2D mapping of facial asymmetry in 3/5 patients. Blue colors are associated with expanded regions relative to contralateral control. Red colors

are associated with regions that display shrinkage compared to contralateral control. Distances (cm) indicate the absolute distance between each node of the affected side and the mirrored non-affected side. Affected side: right. **(C)** Volumetric changes of facial muscles in patients before and after drug introduction. **(D and E)** (D) Representative immunofluorescence of P-AKT^{Thr308} and P-S6RP in healthy contralateral skeletal muscle and (E) in the affected skeletal muscle before and 6 mo after alpelisib introduction. **(F)** Quantification of immunofluorescence intensity. AU: Arbitrary units. Scale bar: 10 µm. Data are shown as mean ± SEM. *P < 0.05 and ***P < 0.001 (two-tailed unpaired *t* test for C and ANOVA, followed by the Tukey–Kramer post hoc test for F). Each dot represents one mouse. Data are representative of at least two independent experiments.

or anatomical structure of interest on PET/CT fusion slices using the PMOD software package (PMOD Technologies Ltd.). FDG accumulation was quantified as the standard uptake value, which measures the ratio of the radioactivity concentration in volume of interest to the whole-body concentration of the injected radioactivity.

Blood and plasma analysis

At the end of each experiment, blood samples were collected from the mice in EDTA-coated tubes. To measure blood count, fresh blood samples were analyzed on a hematology analyzer (ProCyte Dx; IDEXX Laboratories) and centrifuged at 500 × *g* for 15 min. The collected plasma concentration was used to determine insulin (U-PLEX mouse insulin Assay [Meso Scale Discovery], ref# K1526HK) and IGF-1 (ref# MG100; Novus Biologicals) circulating levels using enzymatic methods from commercially available kits.

Oral glucose test

Mice were fasted overnight (12 h) with access to drinking water. All body weights were measured and tails were carefully cut for blood glucose determination (time point 0). During GTT, freshly prepared glucose solution was administered orally (1 g glucose/kg body weight of 20% glucose solution in water; ref# G8270; Sigma-Aldrich). After 15, 30, 45, 60, 90, and 120 min, blood glucose was measured again at all time points.

Morphological analysis

Mouse tissues were fixed in 4% paraformaldehyde and paraffin embedded. Tissue sections (4 µm thick) were stained with hematoxylin and eosin (H&E).

Measurement of muscle fiber size

H&E slides were scanned with a NanoZoomer 2.0HT (Hamamatsu) and analyzed with Qupath-0.2.3 (Bankhead et al., 2017). Muscles were segmented using deep-learning Cellpose algorithm (Stringer et al., 2021). For both, areas were then measured with Fiji (Schindelin et al., 2012).

Immunohistochemistry and immunofluorescence

Paraffin-embedded tissue sections (4 µm) were submitted to antigen retrieval protocols using high temperature (120°C) and high pressure in citrate buffer and a pressure cooker. Sections were then incubated with primary antibodies (Table S1). For the immunofluorescence procedure, appropriate Alexafluor-conjugated secondary antibodies (Thermo Fischer Scientific) were incubated on the samples and analyzed using an LSM 700 confocal microscope (Zeiss) or Eclipse Ni-E (Nikon). Immunohistochemistry revelation was performed with appropriate horseradish peroxidase linked secondary antibodies and analyzed with E800 (Nikon).

In human skin biopsies, P-S6RP and P-AKT^{T308} staining were segmented with Ilastik v1.3.3post3, a machine-learning pixel classification open-source software. For each immunofluorescence staining, mean intensity area and quantity were measured with Fiji v2.3.0/1.53f51 (Quantity = Mean intensity × Area) and normalized by tissue area (Berg et al., 2019).

Western blot

Tissues were crushed and then lysed in radioimmunoprecipitation assay lysis buffer supplemented with phosphatase and protease inhibitors. Protein concentrations were determined through the bicinchoninic acid method (Pierce). Then, protein extracts were resolved by SDS-PAGE before being transferred onto the appropriate membrane and incubated with the primary antibody (Table S1) followed by the appropriate peroxidase-conjugated secondary antibody (dilution 1:10,000). Chemiluminescence was acquired using Chemidoc MP and bands were quantitated using Image Lab Software (Bio–Rad Laboratories).

Tissue digestion

Muscles of *PIK3CA*^{WT} and *PIK3CA*$^{HSA\text{-}CreER}$ mice were harvested and rinsed with PBS 1X (Gibco). After cutting them into small pieces, digestion buffer was added with DNAse (0.1 mg/ml), Dispase I (0.8 mg/ml), and Collagenase P (0.2 mg/ml) in 10 ml of RPMI (Gibco) and incubated for 40 min at 37°C on GentleMACS (Miltenyi) with the appropriate program. Following dissociation, tissues were filtered (70 µm; Clearline), centrifuged 5 min at 250 *g*, and resuspended in PBS.

Mitotracker cytometry

Following treatment with either vehicle or alpelisib, muscle of *PIK3CA*^{WT} and *PIK3CA*$^{HSA\text{-}CreER}$ mice were collected and digested. Cells were resuspended in 100 µl of PBS in a 96-well round-bottomed plate (Thermo Fisher Scientific). Cells were incubated with fluorescent buffer in the dark for 10 min at 37°C (Table S1) and rinsed with PBS-FCS 2%. Cells were analyzed using Sony Spectral ID7000 and all flow data were processed with Sony ID7000 software and Kaluza software.

Imaging flow cytometry (ImageStream)

Skeletal muscles from *PIK3CA*^{WT} and *PIK3CA*$^{HSA\text{-}CreER}$ mice were isolated, rinsed in PBS 1X, cut into small pieces, and digested as detailed below. After dissociation, cell suspensions were filtered (70 µm; Clearline), centrifuged 10 min at 350 *g*, and resuspended in PBD solution 1X supplemented with 2% fetal bovine serum

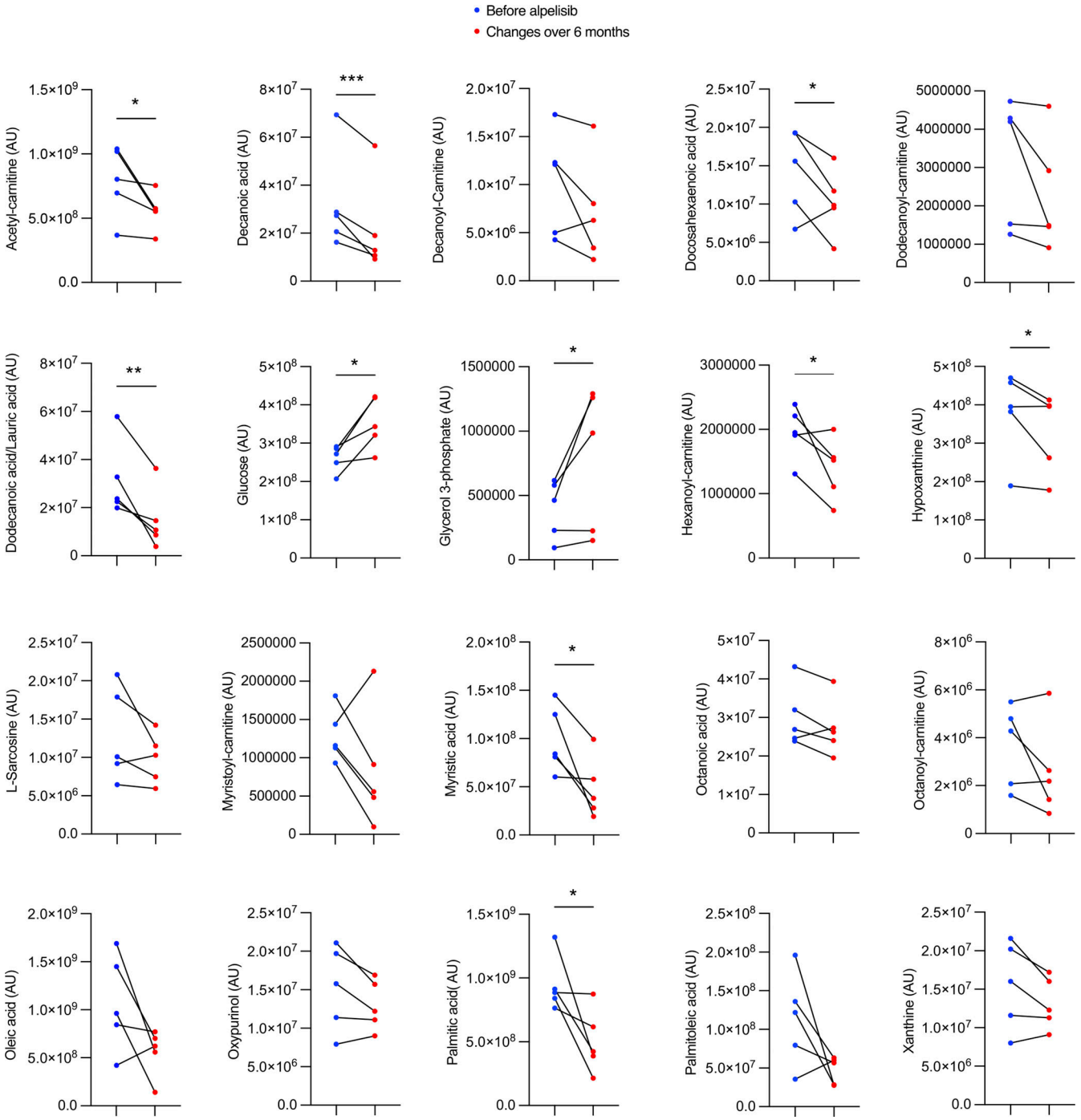

Figure 5. **Metabolic changes observed in patients before and 6 mo after alpelisib introduction.** Graphic example of metabolite level changes observed. AU: Arbitrary units. Data are shown as mean ± sem. *P < 0.05, **P < 0.01, ***P < 0.001 (two-tailed unpaired *t* test).

and EDTA at 0.5 m/mol. Cells were then transferred in a microtube. Samples were run on an ImageStream ISX mkII (Amnis part of Luminex) that combines flow cytometry with detailed cell imaging. Magnification (40×) was used for all acquisitions. Data were acquired with INSPIRE software (Amnis part of Luminex) and analyzed with IDEAS software (v.6.2; Amnis part of Luminex). The antibodies used for flow cytometry are availble in Table S1.

Targeted liquid chromatography–mass spectrometry (LC–MS) metabolites analyses

Plasma and serum were obtained after centrifugation of the blood at 500 *g* for 10 min. Blood samples were obtained in EDTA tubes for plasma analysis and EDTA-free tubes for serum analysis. Cells, plasma, and serum samples were immediately snap-frozen in liquid nitrogen. For the LC–MS analyses, metabolites were extracted as previously described (Ladraa et al.,

2022). Briefly, the extraction solution was composed of 50% methanol, 30% acetonitrile, and 20% water. The volume of the added extraction solution was adjusted to the cell number (1 ml per 1 million cells) or plasma and serum volume (200 µl per 10 µl of plasma or serum). After the addition of extraction solution, samples were vortexed for 5 min at 4°C and then centrifuged at 16,000 *g* for 15 min at 4°C. The supernatants were collected and stored at −80°C until the analyses were performed. LC–MS analyses were conducted using a QExactive Plus Orbitrap mass spectrometer (Thermo Fisher Scientific) equipped with an Ion Max source and a HESI II probe coupled to a Dionex UltiMate 3,000 UPLC system (Thermo Fisher Scientific). External mass calibration was performed using the standard calibration mixture every 7 d as recommended by the manufacturer. 5 µl of each sample was injected onto Zic-pHilic (150 mm × 2.1 mm, 5 µm) with the guard column (20 mm × 2.1 mm, 5 µm; Millipore) for liquid chromatography separation. Buffer A was 20 mM ammonium carbonate and 0.1% ammonium hydroxide (pH 9.2); buffer B was acetonitrile. The chromatographic gradient was run at a flow rate of 0.200 µl/min as follows: for 0–20 min, linear gradient from 80 to 20% B; for 20–20.5 min, linear gradient from 20% to 80% B; for 20.5–28 min, hold at 80% B. The mass spectrometer was operated in full-scan polarity switching mode with the spray voltage set to 2.5 kV and the heated capillary held at 320°C. The sheath gas flow was set to 20 U, the auxiliary gas flow was set to 5 U, and the sweep gas flow was set to 0 U. The metabolites were detected across a mass range of 75–1,000 m/z at a resolution of 35,000 (at 200 m/z) with the automated gain control target set to 106 and a maximum injection time of 250 ms. Lock masses were used to ensure mass accuracy below 5 parts per million. Data were acquired with Thermo Xcalibur 4.0.27.131 software (Thermo Fisher Scientific). The peak areas of metabolites were determined using Thermo TraceFinder 3.3 SP1 software (Thermo Fisher Scientific) and identified by the exact mass of each singly charged ion and by known retention time in the high performance liquid chromatography column.

Patients

HFMH was defined as congenital facial asymmetry with thickening of soft tissues leading to a set of specific clinical features: narrow palpebral fissure, eyebrow ptosis, nose deviation with small alar rim, external ear asymmetry and displacement with prominent concha, chin deviation with skin dimpling, and lip commissure canting. Previous treatment attempts were recorded.

Following procedures previously described (Delestre et al., 2021), the study was conducted on five pediatric patients, including three females who were followed at Hôpital Necker Enfants Malades. This protocol was approved by the Agence Nationale de Sécurité du Médicament et des Produits de Santé and the local ethical committee (Comité d'Éthique de Necker—Enfants Malades). Written informed consent was obtained from adult patients and the parents of pediatric patients. Alpelisib was compassionately offered by Novartis. Patients received 50 mg/d (Venot et al., 2018). Alpelisib was taken orally every morning during breakfast. Patients were assessed at regular intervals as previously reported (Venot et al., 2018). At each visit, 2D photographs were performed for all patients. 3D photographs were performed on three patients (EVA 3D Scanner; Artec 3D). For 3D facial reconstruction, we applied non-rigid and dense registrations between a template and patient faces (Amberg, B. 2007). Each 3D image was rigidly aligned with the template, which was a standardized, controlled, symmetrical mesh of an average human head, using Wrap v2020.12.2 (R3DS) by placing landmarks to control relative positioning and by computing translations, rotations, and scaling (Fig. S1). The template was then warped around the 3D face by computing a non-rigid iterative closest point alignment involving 50 iterations. The deformed template mesh had the target mesh shape and preserved its original node topology. The 3D coordinates of all nodes were extracted and processed in R (R Core Team, 2018), where the node coordinates were aligned based on Procrustes superimposition without scaling using ProcSym from Morpho library (Schlager, 2017). The superimposition included only the non-affected side of the face to emphasize the variations located on the affected side. PLS2B were computed to screen for covariation patterns described by Procrustes coordinates and time since treatment introduction using PLS2B from the Morpho library (Schlager, 2017). The theoretical morphological changes associated with each statistically significant covariation axis were visualized using tps3d from the Morpho (Schlager, 2017) and shade3d from the rgl library (Murdoch and Adler, 2023). Non-affected sides were mirrored based on sagittal planes using Wrap and the Procrustes distances between the affected and the mirrored non-affected sides were computed, leading to the generation of facial heatmaps (Fig. S1) using meshDist from the Morpho library (Schlager, 2017). 2D photographs were analyzed as previously described (Hennocq et al., 2023). After manual landmarking, clouds of landmarks were extracted from the frontal views (n = 105), profile views (n = 73), and external ears (n = 41) and compared after Procrustes superimposition and principal component analysis. The pretreatment facial phenotype was compared to the facial phenotype after a minimum of 6 mo of treatment. Analyses were performed in R (R Core Team, 2018) using the geomorph package.

In addition, we assessed the volume of skeletal muscle overgrowth using MRI for each patient. MRI examination was performed using T1, T2, and fat suppression, and T2-weighted imaging sequences were performed before alpelisib (day 0) introduction and again 6 mo after. Volumetric evaluation of skeletal muscle malformation was determined by thresholding and manually delineating hypersignal T2 lesions. Volume was calculated by summing images based on the 2D contours and slice thickness.

Biopsies of the buccinator and/or masseter muscles of the affected and control sides were performed in 5/5 HFMH patients, for diagnosis, and four out of five patients after 6 mo of treatment.

Control buccinator and masseter muscles were harvested on pediatric patients admitted for facial lacerations and/or mandibular trauma, that required surgical approaches to this anatomical region.

Data analysis and statistics

Data are expressed as the means ± SEM. Differences between the experimental groups were evaluated using ANOVA, followed by the Tukey–Kramer post hoc test when the results were significant ($P < 0.05$). When only two groups were compared, Mann–Whitney tests were used. Statistical analyses were performed using GraphPad Prism software (version 10.0.0).

Online supplemental material

Fig. S1 shows the workflow for the assessment of 3D pictures. Fig. S2 shows the mouse model characterization and quantitative histological analysis of tibialis anterior muscle changes in *PIK3CA*^{WT} and *PIK3CA*$^{HSA\text{-}CreER}$ mice treated with either vehicle or alpelisib. Fig. S3 shows metabolic changes observed in *PIK3CA*^{WT} and *PIK3CA*$^{HSA\text{-}CreER}$. Fig. S4 shows metabolic changes observed in *PIK3CA*^{WT} and *PIK3CA*$^{HSA\text{-}CreER}$ treated with either vehicle or alpelisib. Fig. S5 shows the covariation between treatment duration and facial asymmetry using two-blocks partial least-squares regressions. Table S1 lists the antibodies, materials, and buffers used in the study.

Data availability

All data needed to evaluate the conclusions in the paper are present in the paper and/or the supplementary materials.

Acknowledgments

We are very grateful to our generous donors.

This study was supported by the European Research Council (CoG 2020 grant number 101000948 awarded to G. Canaud), the Agence Nationale de la Recherche—Programme d'Investissements d'Avenir (ANR-18-RHUS-005 to G. Canaud), and the Agence Nationale de la Recherche—Programme de Recherche Collaborative (19-CE14-0030-01 to G. Canaud). This work was also supported by the CLOVES Syndrome Community (West Kennebunk, USA), Association Syndrome de CLOVES (Nantes, France), Fondation d'entreprise IRCEM (Roubaix, France), Fonds de dotation Emmanuel Boussard (Paris, France), the Fondation Day Solvay (Paris, France), the Fondation TOURRE (Paris, France) to G. Canaud, the Fondation Bettencourt Schueller (Paris, France) to G. Canaud, the Fondation Simone et Cino Del Duca (Paris, France), the Fondation Line Renaud-Loulou Gaste (Paris, France), the Fondation Schlumberger pour l'Education et la Recherche (Paris, France), the Fondation Maladies Rares, the Association Robert Debré pour la Recherche Médicale awarded to G. Canaud, WonderFIL Smiles (Norway), Institut national de la santé et de la recherche médicale, Assistance Publique Hôpitaux de Paris and Université Paris Cité. In vivo preclinical imaging was performed at the Life Imaging Facility of the University of Paris (Plateforme Imageries du Vivant), supported by France Life Imaging (grant ANR-11-INBS-0006) and Infrastructures BiologieSanté.

Author contributions: C. Bayard, B. Periou, L. Zerbib, and S. Ladraa performed the experiments, analyzed the data, and elaborated figures. E. Segna, C. Broissand, C. Legendre, C. Gitiaux, B. Sergent, and A. Picard followed patients and participated in data analysis. M. Taverne and Q. Hennocq analyzed 2D and 3D photographs. A. Fraissenon, L. Guibaud, G. Autret, and B. Tavitian designed and analyzed MRI experiments. C. Chapelle and C. Hoguin were in charge of mice experiments including genotyping, breeding, tamoxifen administration, and sacrifice. V. Asnafi, S. Kaltenbach, and P. Villarese performed molecular diagnosis in patients. F.-J. Authier, S. Fraitag, and J.-P. Duong analyzed mice and human tissues section. I. Nemazanyy performed the metabolomic analysis. C. Delcros helped with some of the in vivo experiments. T. Viel performed the FDG uptake experiments. N. Goudin analyzed and quantified immunofluorescence expression in tissues. M. Dussiot provided help for flow cytometry experiments. R. Khonsari and G. Canaud followed the patients, provided the conceptual framework, designed the study, supervised the project, and wrote the paper.

Disclosures: B. Periou reported benefitting from fellowship from the Agence Nationale pour la Recherche (RHU CARMMA, ANR-15-RHUS-OOO3). F.-J. Authier reported benefitting from research grants from the Association Française contre les Myopathies via TRANSLAMUSCLE (PROJECT 19507 and 22946) and the Agence Nationale pour la Recherche (RHU CARMMA, ANR-15-RHUS-0003). G. Canaud reported personal fees from Novartis, Vaderis, Ipsen, BridgeBio, and Alkermes outside the submitted work; in addition, G. Canaud had a patent to WO2017140828A1 licensed to Novartis. No other disclosures were reported.

Submitted: 29 May 2023
Revised: 19 July 2023
Accepted: 9 August 2023

References

Amberg, B. 2007. Conference on Computer Vision and Pattern Recognition. IEEE, Minneapolis, MN, USA. 1–8.

Bankhead, P., M.B. Loughrey, J.A. Fernández, Y. Dombrowski, D.G. McArt, P.D. Dunne, S. McQuaid, R.T. Gray, L.J. Murray, H.G. Coleman, et al. 2017. QuPath: Open source software for digital pathology image analysis. *Sci. Rep.* 7:16878. https://doi.org/10.1038/s41598-017-17204-5

Berg, S., D. Kutra, T. Kroeger, C.N. Straehle, B.X. Kausler, C. Haubold, M. Schiegg, J. Ales, T. Beier, M. Rudy, et al. 2019. Ilastik: Interactive machine learning for (bio)image analysis. *Nat. Methods.* 16:1226–1232. https://doi.org/10.1038/s41592-019-0582-9

Canaud, G., A.M. Hammill, D. Adams, M. Vikkula, and K.M. Keppler-Noreuil. 2021. A review of mechanisms of disease across PIK3CA-related disorders with vascular manifestations. *Orphanet J. Rare Dis.* 16:306. https://doi.org/10.1186/s13023-021-01929-8

Castillo Taucher, S., R.A. Pardo Vargas, and D. Caivi León. 2003. Hemifacial myohyperplasia: An additional case. *Am. J. Med. Genet. A.* 116A:103–104. https://doi.org/10.1002/ajmg.a.10839

Delestre, F., Q. Venot, C. Bayard, A. Fraissenon, S. Ladraa, C. Hoguin, C. Chapelle, J. Yamaguchi, R. Cassaca, L. Zerbib, et al. 2021. Alpelisib administration reduced lymphatic malformations in a mouse model and in patients. *Sci. Transl. Med.* 13:eabg0809. https://doi.org/10.1126/scitranslmed.abg0809

Fedorov, A., R. Beichel, J. Kalpathy-Cramer, J. Finet, J.C. Fillion-Robin, S. Pujol, C. Bauer, D. Jennings, F. Fennessy, M. Sonka, et al. 2012. 3D slicer as an image computing platform for the quantitative imaging network. *Magn. Reson. Imaging.* 30:1323–1341. https://doi.org/10.1016/j.mri.2012.05.001

Hennocq, Q., T. Bongibault, M. Bizière, O. Delassus, M. Douillet, V. Cormier-Daire, J. Amiel, S. Lyonnet, S. Marlin, M. Rio, et al. 2023. An automatic facial landmarking for children with rare diseases. *Am. J. Med. Genet. A.* 191:1210–1221. https://doi.org/10.1002/ajmg.a.63126

Klippel, A., C. Reinhard, W.M. Kavanaugh, G. Apell, M.A. Escobedo, and L.T. Williams. 1996. Membrane localization of phosphatidylinositol 3-kinase

is sufficient to activate multiple signal-transducing kinase pathways. *Mol. Cell. Biol.* 16:4117–4127. https://doi.org/10.1128/MCB.16.8.4117

Ladraa, S., L. Zerbib, C. Bayard, A. Fraissenon, Q. Venot, G. Morin, A.P. Garneau, P. Isnard, C. Chapelle, C. Hoguin, et al. 2022. PIK3CA gain-of-function mutation in adipose tissue induces metabolic reprogramming with Warburg-like effect and severe endocrine disruption. *Sci. Adv.* 8: eade7823. https://doi.org/10.1126/sciadv.ade7823

Lee, S., R. Sze, C. Murakami, J. Gruss, and M. Cunningham. 2001. Hemifacial myohyperplasia: Description of a new syndrome. *Am. J. Med. Genet.* 103: 326–333. https://doi.org/10.1002/1096-8628(20011101)103:4<326::AID-AJMG1578>3.0.CO;2-Z

Li, M.E., H.P.M.M. Lauritzen, B.T. O'Neill, C.-H. Wang, W. Cai, B.B. Brandao, M. Sakaguchi, R. Tao, M.F. Hirshman, S. Softic, et al. 2019. Role of p110a subunit of PI3-kinase in skeletal muscle mitochondrial homeostasis and metabolism. *Nat. Commun.* 10:3412. https://doi.org/10.1038/s41467-019-11265-y

Madsen, R.R. and B. Vanhaesebroeck. 2020. Cracking the context-specific PI3K signaling code. *Sci Signal,* 13:eaay2940. https://doi.org/10.1126/scisignal.aay2940

Miranda, R.T., L.M. Barros, L.A. Santos, P.R. Bonan, and H. Martelli Jr. 2010. Clinical and imaging features in a patient with hemifacial hyperplasia. *J. Oral Sci.* 52:509–512. https://doi.org/10.2334/josnusd.52.509

Morin, G., C. Degrugillier-Chopinet, M. Vincent, A. Fraissenon, H. Aubert, C. Chapelle, C. Hoguin, F. Dubos, B. Catteau, F. Petit, et al. 2022. Treatment of two infants with PIK3CA-related overgrowth spectrum by alpelisib. *J. Exp. Med.* 219:e20212148. https://doi.org/10.1084/jem.20212148

Murdoch, D., and D. Adler. 2023. Rgl: 3D visualization using openGL. https://birs.ok.ubc.ca/wjbraun/DS550/lecture7.html

Muzumdar, M.D., B. Tasic, K. Miyamichi, L. Li, and L. Luo. 2007. A global double-fluorescent Cre reporter mouse. *Genesis.* 45:593–605. https://doi.org/10.1002/dvg.20335

Pereira-Perdomo, D.F., J. Vélez-Forero, and R. Prada-Madrid. 2010. Hemifacial myohyperplasia sequence. *Am. J. Med. Genet. A.* 152A:1770–1773. https://doi.org/10.1002/ajmg.a.33428

R Core Team. 2018. R: A Language and Environment for Statistical Computing. R Foundation for Statistical Computing, Vienna, Austria.

Schindelin, J., I. Arganda-Carreras, E. Frise, V. Kaynig, M. Longair, T. Pietzsch, S. Preibisch, C. Rueden, S. Saalfeld, B. Schmid, et al. 2012. Fiji: An open-source platform for biological-image analysis. *Nat. Methods.* 9: 676–682. https://doi.org/10.1038/nmeth.2019

Siponen, M., G.K.B. Sándor, L. Ylikontiola, T. Salo, and H. Tuominen. 2007. Multiple orofacial intraneural perineuriomas in a patient with hemifacial hyperplasia. *Oral Surg. Oral Med. Oral Pathol. Oral Radiol. Endod.* 104:e38–e44. https://doi.org/10.1016/j.tripleo.2006.12.030

Schlager, S. 2017. Morpho and rvcg – shape analysis in R. In Statistical Shape and Deformation Analysis. G. Zheng, S. Li, and G. Szekely, editors. Academic Press, Cambridge, MA. 217–256. https://doi.org/10.1016/B978-0-12-810493-4.00011-0

Srinivasan, L., Y. Sasaki, D.P. Calado, B. Zhang, J.H. Paik, R.A. DePinho, J.L. Kutok, J.F. Kearney, K.L. Otipoby, and K. Rajewsky. 2009. PI3 kinase signals BCR-dependent mature B cell survival. *Cell.* 139:573–586. https://doi.org/10.1016/j.cell.2009.08.041

Stringer, C., T. Wang, M. Michaelos, and M. Pachitariu. 2021. Cellpose: A generalist algorithm for cellular segmentation. *Nat. Methods.* 18: 100–106. https://doi.org/10.1038/s41592-020-01018-x

Venot, Q., T. Blanc, S.H. Rabia, L. Berteloot, S. Ladraa, J.P. Duong, E. Blanc, S.C. Johnson, C. Hoguin, O. Boccara, et al. 2018. Targeted therapy in patients with PIK3CA-related overgrowth syndrome. *Nature.* 558: 540–546. https://doi.org/10.1038/s41586-018-0217-9

Zissman, S., Y. Cooperman, D. Leshem, and E. Gur. 2020. Progressive surgical management of hemifacial myohyperplasia for improved functional and aesthetic results. *Plast. Reconstr. Surg. Glob. Open.* 8:e2724. https://doi.org/10.1097/GOX.0000000000002724

JEM

Supplemental material

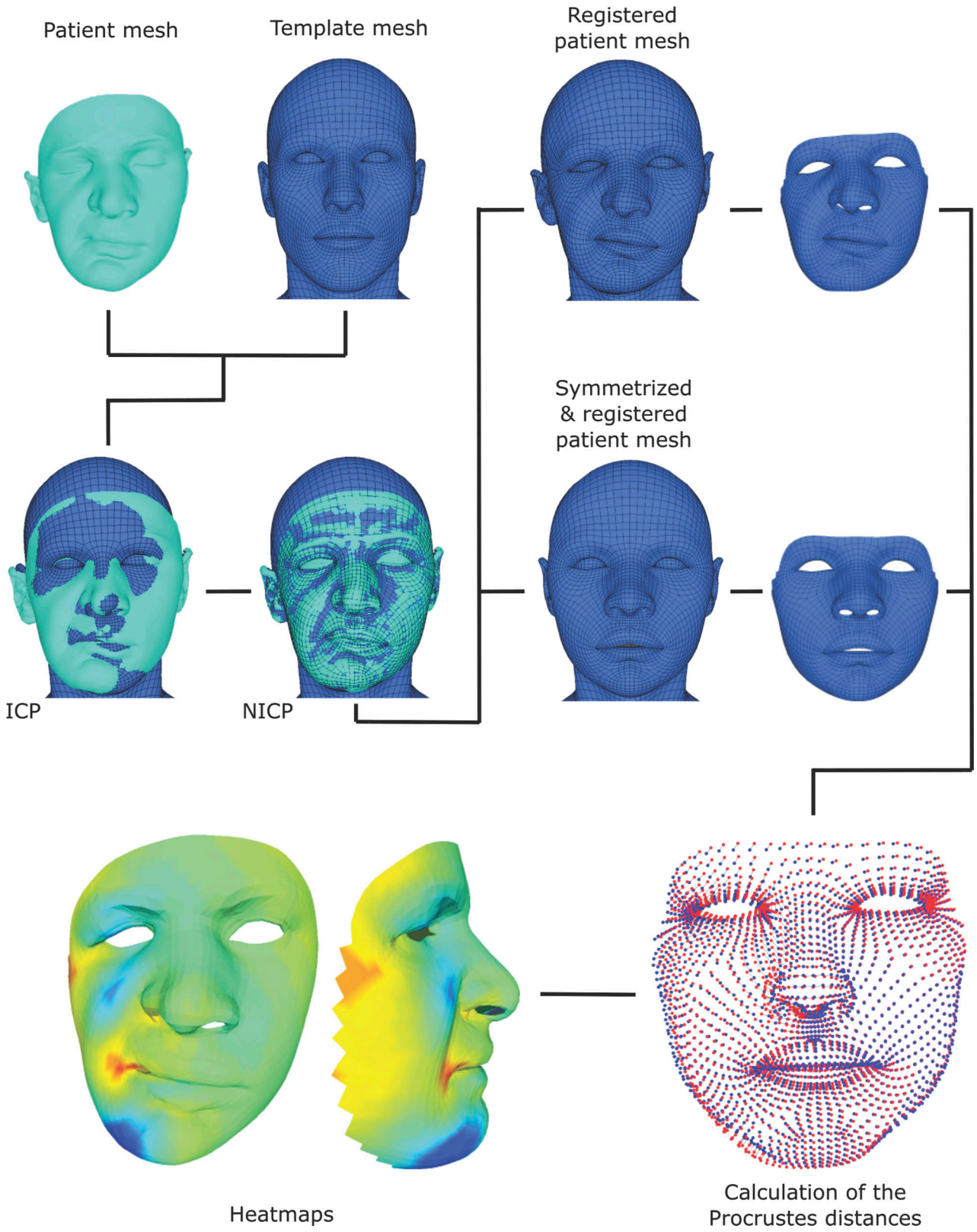

Figure S1. **Workflow for the assessment of 3D pictures.** First, the template (blue mesh) was rigidly matched with the "target" head surface of each patient (cyan mesh) by an ICP (iterative closest point) alignment. The template was then non-rigidly matched with the target surface by means of an NICP (non-rigid iterative closest point) alignment, which consists of the local deformation of the template following thin-plate splines to adopt the conformation of the target. This resulted in a registered template. The process was repeated for each subject at each age. Then, the facial region was extracted and symmetrized against the non-affected facial side. A Procrustes superimposition was performed to align all faces to tackle undesirable effects of position and orientation. Finally, all subsequent analyses including the generation of heatmaps were computed on the Procrustes coordinates exclusively.

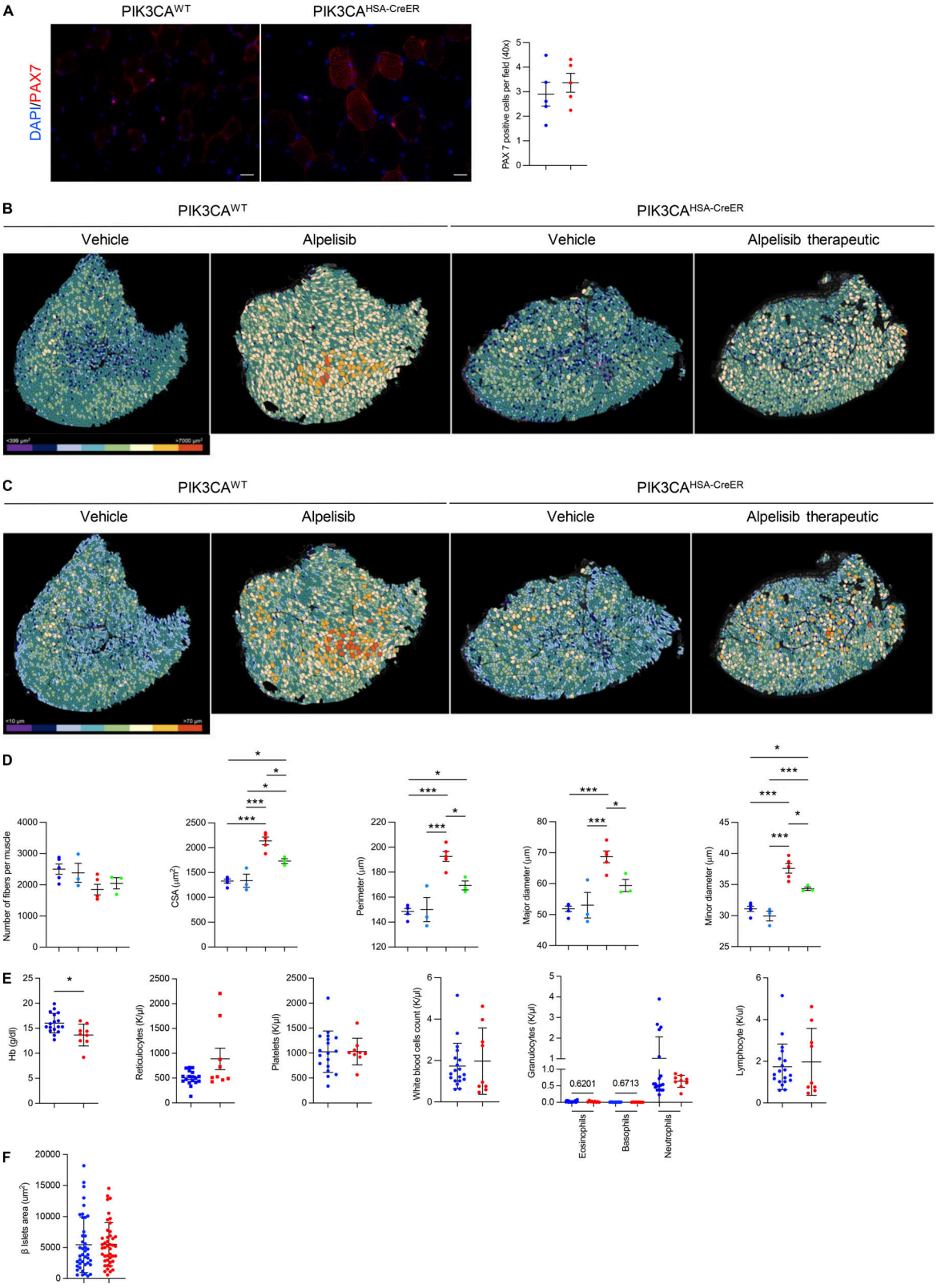

Figure S2. **Mouse model characterization and quantitative histological analysis of tibialis anterior (TA) muscle changes in *PIK3CA*^{WT} and *PIK3CA*$^{HSA\text{-}CreER}$ mice treated with either vehicle or alpelisib. (A)** Representative immunofluorescence of PAX7 satellite cells and quantification. **(B and C)** Digital pictures of TA muscle cross-section area allowing an automated image quantification of (B) major and minor (C) myofiber diameters in *PIK3CA*^{WT} and *PIK3CA*$^{HSA\text{-}CreER}$ mice treated with either vehicle or alpelisib. **(D)** Quantification. **(E)** Complete blood count in *PIK3CA*^{WT} and *PIK3CA*$^{HSA\text{-}CreER}$ mice. **(F)** β Islet area in *PIK3CA*^{WT} and *PIK3CA*$^{HSA\text{-}CreER}$ mice. Data are shown as mean ± SEM. *P < 0.05 and ***P < 0.001 (two-tailed unpaired *t* test for A, E, and F, and ANOVA, followed by the Tukey–Kramer post hoc test for D). Each dot represents one mouse. Data are representative of at least two independent experiments.

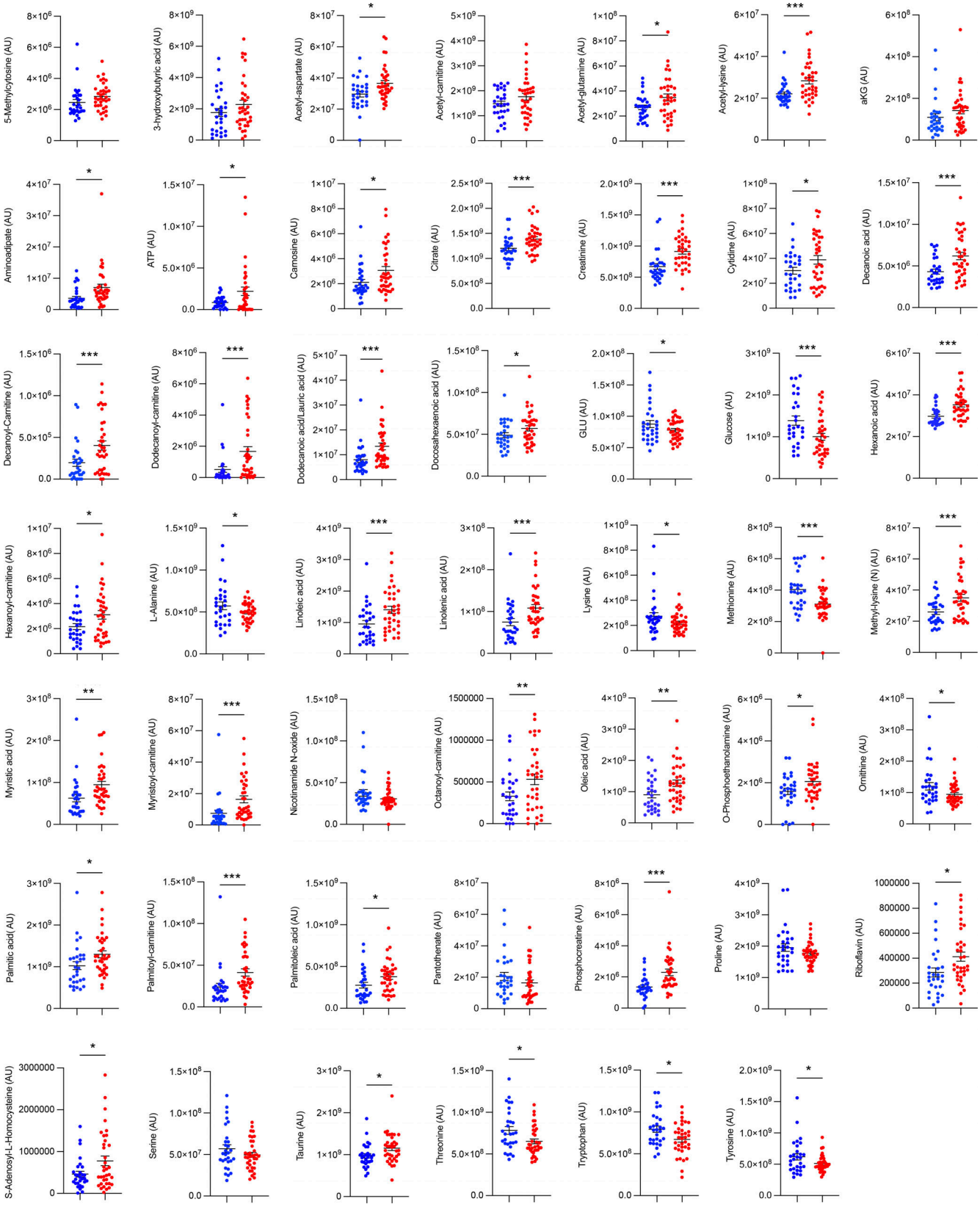

Figure S3. **Metabolic changes observed in *PIK3CA*^{WT} and *PIK3CA*$^{HSA\text{-}CreER}$.** Graphic example of metabolite level changes observed. AU: Arbitrary units. Data are shown as mean ± SEM. *P < 0.05, **P < 0.01, ***P < 0.001 (two-tailed unpaired *t* test).

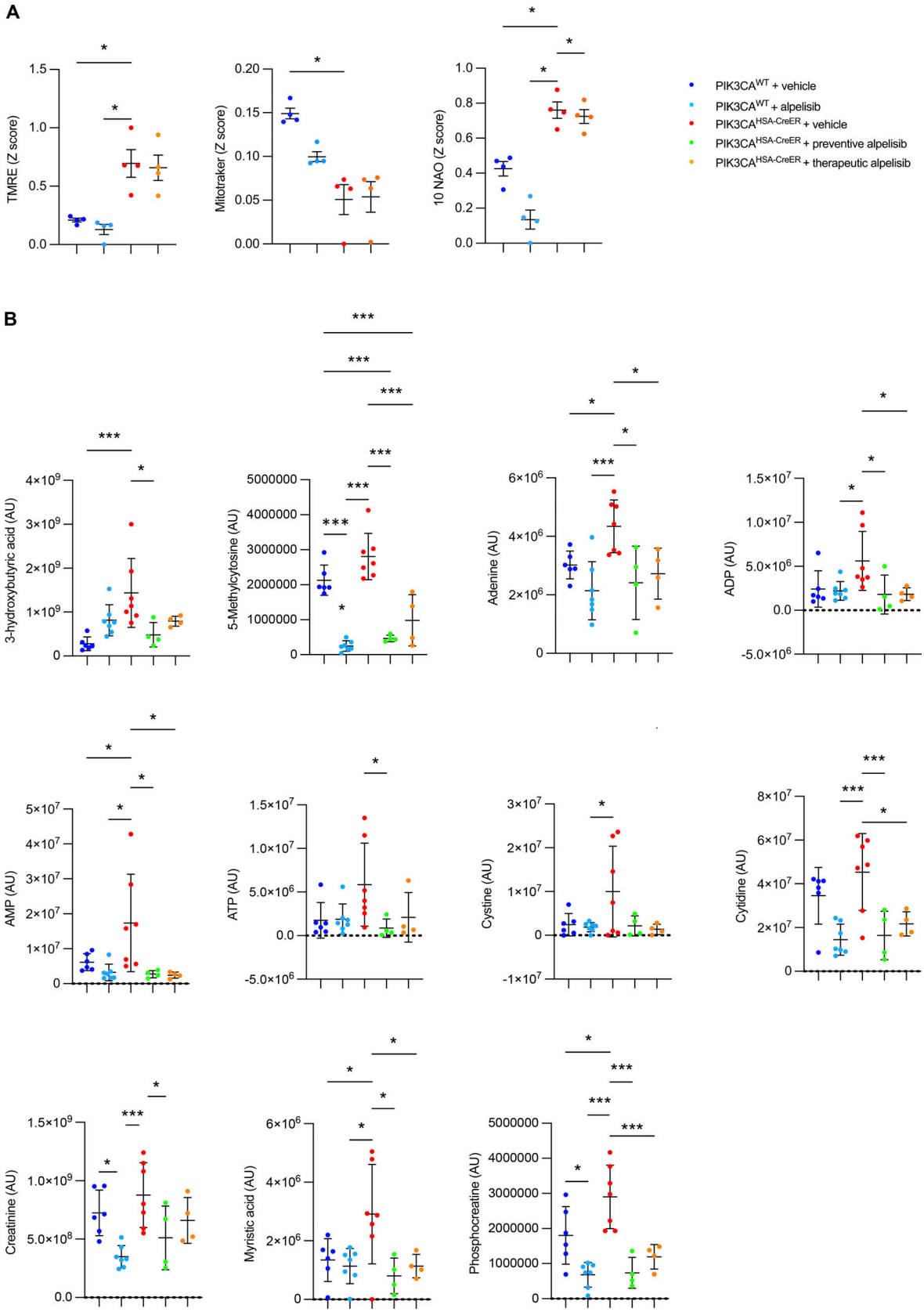

Figure S4. **Metabolic changes observed in *PIK3CA*^{WT} and *PIK3CA*$^{HSA\text{-}CreER}$ treated with either vehicle or alpelisib. (A)** TMRE, Mitotraker, and 10 NAO staining in skeletal muscle of *PIK3CA*^{WT} and *PIK3CA*$^{HSA\text{-}CreER}$ mice treated with either vehicle or alpelisib (n = 4 per group). **(B)** Graphic example of metabolite level changes observed (n = 4–7 per group). AU: Arbitrary units. Data are shown as mean ± sem. *P < 0.05 and ***P < 0.001 (ANOVA, followed by the Tukey–Kramer post hoc test).

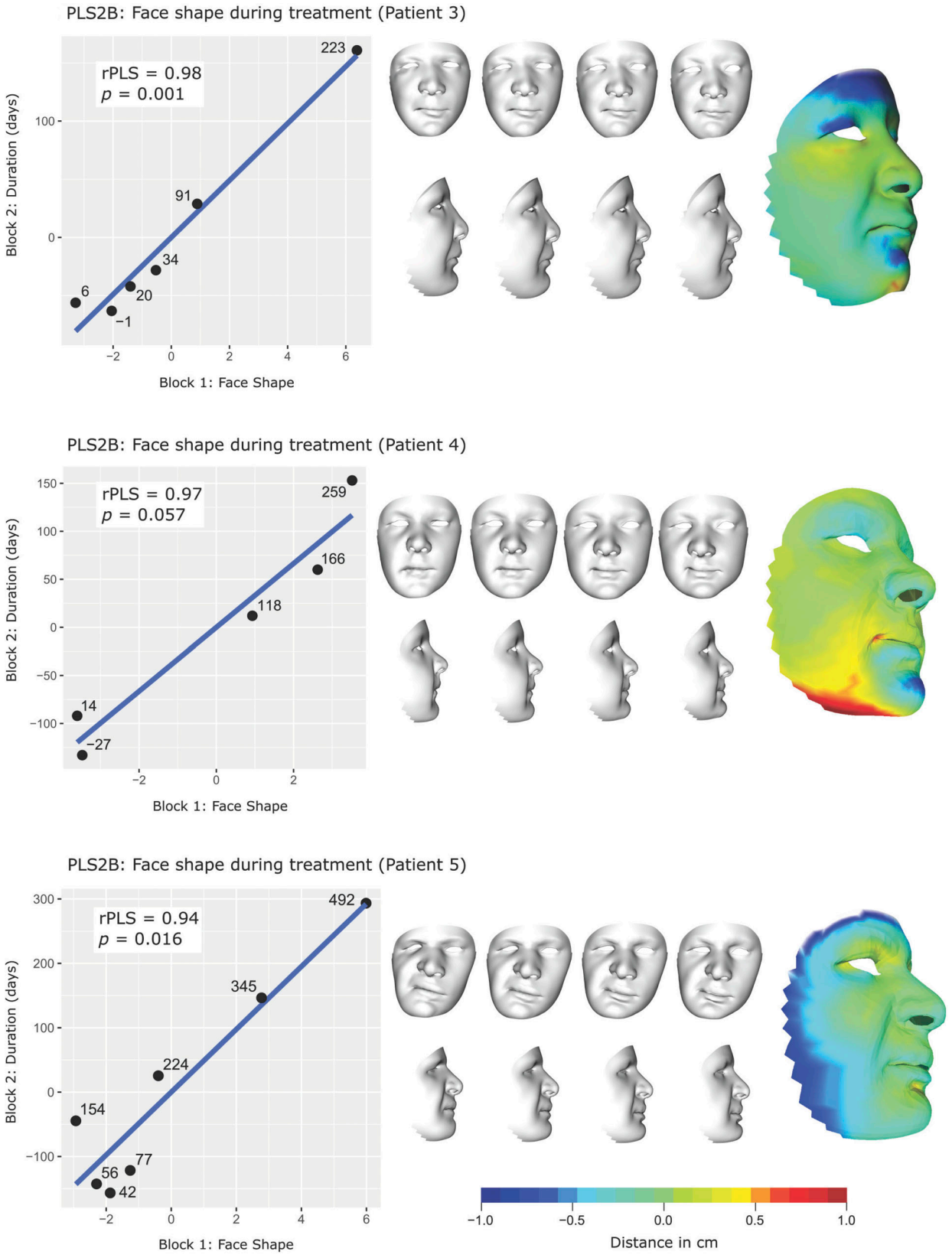

Figure S5. **Covariation between treatment duration and facial asymmetry using PLS2B.** PLS2B assessing the covariation between facial morphology (Block 1) and treatment duration (Block 2) in 3/5 patients. rPLS: coefficient of covariation; p: P value; each point represents a 3D face mesh annotated with the duration, in days, since treatment onset. White faces represent the theoretical face deformation along with the covariation axis (from the left to the right: from the start of the treatment, until the most recent 3D picture). Rightmost is a heatmap representation of the main facial regions corrected by the treatment. Colder colors pinpoint expanded regions, whereas hotter colors pinpoint shrunk regions.

Provided online is Table S1, which lists antibodies, materials, and buffers used in the study.